Article

Partial Oxidation Strategy to Synthesize WS$_2$/WO$_3$ Heterostructure with Enhanced Adsorption Performance for Organic Dyes: Synthesis, Modelling, and Mechanism

Guiping Li [1]**, Yongli Wang** [1,2,]*****, Jingtao Bi** [1] **, Xin Huang** [1,2] **, Yafei Mao** [1]**, Liang Luo** [1] **and Hongxun Hao** [1,2,]*****

[1]   National Engineering Research Center for Industry Crystallization Technology, School of Chemical Engineering and Technology, Tianjin University, Tianjin 300072, China; ligp@tju.edu.cn (G.L.); jingtaob@gmail.com (J.B.); x_huang@tju.edu.cn (X.H.); maoyafei@tju.edu.cn (Y.M.); 2016207086@tju.edu.cn (L.L.)

[2]   Co-Innovation Center of Chemical Science and Engineering, Tianjin 300072, China

*****   Correspondence: yliwang@tju.edu.cn (Y.W.); hongxunhao@tju.edu.cn (H.H.)

check for updates

Abstract: In this work, a facile oxidation strategy was developed to prepare novel tungsten disulfide/tungsten trioxide (WS$_2$/WO$_3$) heterostructures for adsorbing organic dyes efficiently by combining the hydrophilic property of WO$_3$ and the superior dye affinity of WS$_2$. The structural and elemental properties of the synthesized hybrid materials were systematically investigated, and the results demonstrated the retained flower-like morphology of the primitive WS$_2$ and the successful introduction of WO$_3$. Furthermore, surface properties such as a superior hydrophilicity and negative-charged potential were also demonstrated by a water contact angle characterization combined with a Zeta potential analysis. The performance of the obtained WS$_2$/WO$_3$ hybrid materials for removing Rhodamine B (RhB) from wastewater was evaluated. The results showed that the maximum adsorption capacity of the newly synthesized material could reach 237.1 mg/g. Besides, the adsorption isotherms were also simulated by a statistical physics monolayer model, which revealed the non-horizontal orientation of adsorbates and endothermic physical interaction. Finally, the adsorption mechanism and the recyclability revealed that the partial oxidation strategy could contribute to a higher adsorption capacity by modulating the surface properties and could be applied as a highly efficient strategy to design other transition metal dichalcogenides (TMDs) heterostructures for removing organic dyes from wastewater.

Keywords: WS$_2$/WO$_3$ heterostructure; surface property; partial oxidation; hydrophilicity; adsorption mechanism

1. Introduction

In the past several decades, it was estimated that millions of tons of dyes were produced annually, and amount of dyes were discarded into water as waste [1–3]. These organic dyes, which are toxic, non-biodegradable, and even carcinogenic, had posed serious threats to human health and marine organisms [4]. Consequently, it is urgent to develop low-cost and efficient methods to remove these organic dyes from wastewater. Various technologies have been developed and employed for treating wastewater, including membrane filtration, electrochemical decolorization, photocatalytic degradation, chemical oxidation/reduction, biodegradation, and adsorption [2,5–15]. Among them, adsorption is considered a promising candidate to eliminate dyes from industrial wastewater due to the low capital

cost, simplicity of operation, and low introduction of toxic byproducts. A large number of materials have been developed and utilized in adsorption, such as carbon nanotubes, metal-organic framework (MOF), and graphene, which have the advantages of a high surface area, hydrophilic properties, and intense interactions between adsorbents and adsorbates [4,16–21].

Recently, materials with a layered structure started to be investigated and applied in the field of adsorption. They have already shown unique chemical and physical advantages compared with the bulk counterparts since the layered structures possess open channels to provide more active sites for adsorbates. Among these materials, the transition metal dichalcogenides (TMDs) are attractive due to their sandwich structures where covalently bound (X–M–X) trilayers are held together by van der Waals forces, which are conducive to forming a layered structure [22,23]. More importantly, strong polar X–S covalent bonds located at lamellar layers' edges could attract polar species like organic dyes [22,24]. However, the layer nanosheets are inevitably restacked and agglomerated owing to their high surface energy, which would result in the decrement of adsorption sites and the corresponding adsorption effect [25]. Therefore, some studies were conducted to assemble 2D nanosheets in hierarchical three-dimensional (3D) structures to prevent their restacking or agglomeration. For example, 3D flower-like MoS_2 synthesized by Geng et al. exhibited a maximum adsorption capacity of 49.2 mg/g for RhB dye [26]. Furthermore, He et al. introduced porosity into the flower-like MoS_2 adsorbents, resulting in an increment of the adsorption capacity for RhB (163 mg/g), with an extension of the adsorption duration [27]. These reported investigations mainly concentrated on MoS_2 whereas other TMD materials are still less explored. Moreover, most reported studies were primarily focused on the construction of different 3D structures, while investigations on the surficial modification are limited.

In this study, WS_2, a typical TMD material with a similar structure to MoS_2 was selected as the model material to study the relationship between surficial modification and adsorption behavior. Herein, *N*-methy-l-2-pyrrolidone (NMP) was applied as the solvent medium to enhance the vulcanization of WCl_6, and a partial oxidation method was introduced to modulate the surficial conditions of WS_2 to synthesize WS_2/WO_3 hybrid materials. Besides, characterizing methods including scanning electron microscopy (SEM), transmission electron microscopy (TEM), X-ray diffraction (XRD), X-ray photoelectron spectroscopy (XPS), Fourier transform infrared (FTIR) spectra, Zeta potential, and contact angle measurements were utilized to confirm the successful fabrication of WS_2/WO_3 heterostructures and to explore the properties of surface charges and hydrophilicity after partial oxidation. Furthermore, batch absorption experiments were systematically conducted, and a synergistic effect between the hydrophilic property of WO_3 and superior dye affinity of WS_2 was observed. Finally, the adsorption kinetics and isotherms were investigated to better understand the adsorption process, and the adsorption mechanism was revealed.

2. Materials and Methods

2.1. Materials

Tungsten hexachloride (WCl_6, ≥99 wt% purity), N-methyl-2-pyrrolidone (NMP, ≥99.5% purity), sublimed sulfur (S, 99.5 wt% purity), and Rhodamine B (99 wt% purity) were purchased from Aladdin Co., Ltd. (Shanghai, China). NaOH (96.0 wt% purity) and HNO_3 (68 wt% purity) were purchased from Tianjin Kermel Co., Ltd. (Tianjin, China). All reagents were used as received without further purification, and ultra-pure water was prepared in our laboratory and used throughout.

2.2. Synthesis of WS_2, WS_2/WO_3 Heterostructures and WO_3

The preparation procedures of WS_2, WS_2/WO_3 hybrids, and WO_3 are illustrated in Figure 1. The WS_2 microflowers were first synthesized by using a solvothermal method [28]. In general, WCl_6 (0.894 g) was dissolved in NMP (70 mL), and this suspension was stirred for 10 min to obtain a dark brown solution. Next, sublimed sulfur was added into the mixture accompanied with an ultrasonic treatment for 20 min until a homogenous solution was formed. Subsequently, the solution was

transferred into a 100 mL PolyPhenyLene-lined stainless steel autoclave and was heated at 240 °C for 20 h. After the solvothermal process, the black precipitates were collected and dried under vacuum at 100 °C for 12 h. The black powder was WS_2 and was thereafter annealed at 850 °C for 2 h under argon atmosphere to increase the crystallinity.
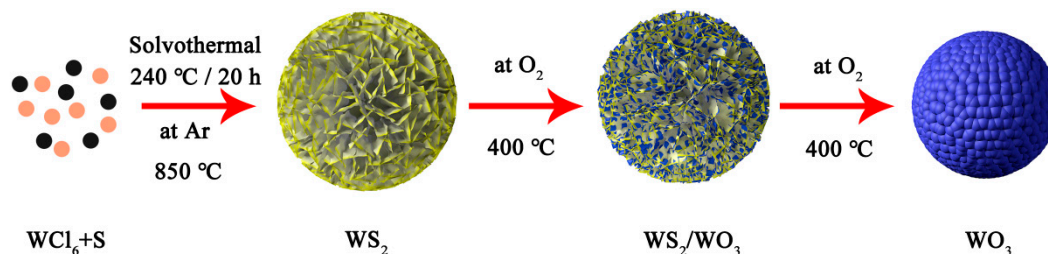
Figure 1. Schematic illustration of the synthetic procedure of WS_2, WS_2/WO_3, and WO_3.

After the synthesis of WS_2, the solids were treated in a furnace at 400 °C for n (n = 5, 30, and 60) min under oxygen flow (100 mL/min) to obtain a series of partially oxidized products which were denoted as WSO-n. Finally, pure WO_3 was obtained with an extending duration of 4 h.

2.3. Material Characterizations

X-ray diffraction patterns of the obtained materials were recorded by an X-ray powder diffractometer (D/max 2500, Rigaku, Tokyo, Japan) with Cu Kα radiation (λ = 1.5418 Å). A thermal gravimetric analysis (TGA) was performed under oxygen flow on a NETZSCH TG 209F3 analyzer (Bavaria, Germany). Morphological information was recorded by scanning electron microscopy (Nanosem 430, FEI, Eindhoven, Netherlands) and transmission electron microscopy (Tecnai G^2 F20, FEI, Eindhoven, Netherlands). Elements contents and their chemical states were analyzed by X-ray photoelectron spectroscopy (ESCALAB 250XI, Al Kα, Thermo, MA, USA) which was calibrated by contaminant carbon at 284.8 eV. Zeta potentials were analyzed by Malvern Zetasizer Nano Series (Nano ZSP, Malvern, Worcestershire, UK) in the pH range of 10 to 2. The Fourier transform infrared (FTIR) spectra with the wavelength range of 4000–400 cm^{-1} were obtained using a Bruker Alpha spectrometer (Regensburg, Germany). Water contact angles were measured on a Dataphysics OCA contact angle meter.

2.4. Batch Adsorption Experiments

All the following adsorption experiments except the adsorption isotherms were conducted at 30 °C. The kinetic studies of different obtained materials toward the absorption of RhB were investigated via the following procedure: 20 mg of adsorbents were put into a 40 mL RhB solution (200 mg/L), after which the mixture was placed in a dark place and stirred vigorously. The mixture was sampled at predetermined time intervals, and then the solid absorbent was separated from the solution through centrifugation. The concentration of the remaining RhB dye on solution was measured via a UV–vis spectrophotometer (Hitachi U4100 spectrophotometer, Kyoto, Japan), at the maximum adsorption wavelength of RhB (554 nm). The adsorption amount Q_t (mg/g) of RhB was expressed as follows:

$$Q_t = \frac{(C_0 - C_t)V}{m}, \tag{1}$$

where C_0 and C_t (mg/L) represent the concentrations of remaining RhB at times 0 and t (min), respectively. V (L) is the volume of RhB solution, and m (g) is the mass of the adsorbent.

The adsorption isotherms of RhB on WSO-5 were conducted at 30, 40, and 50 °C with a solution pH of 6. Specifically, the adsorption experiments were performed by putting 20 mg of the as-prepared materials into a 40 mL RhB solution with different concentrations (100–400 mg/L) under a constant

stirring rate of 200 rpm. After adsorption for 5 h to reach the equilibrium condition, the solid phase was separated from the liquid phase by centrifugation, and the equilibrium concentration of RhB was measured. The relative adsorption capacity of RhB was calculated by the following formula:

$$Q_e = \frac{(C_0 - C_e)V}{m}, \tag{2}$$

where Q_e (mg/g) represents the equilibrium adsorption capacity of RhB, and C_e (mg/L) is the concentration of RhB at equilibrium status.

The effect of the pH was explored by adding 20 mg adsorbent into a 40 mL RhB solution (200 mg/L) at a series of pH levels (10 to 2). The required pH values were adjusted by adding a negligible volume of 0.1 M HNO_3 and NaOH solutions. Furthermore, the effect of the adsorbent dosage was also studied by conducting a 40 mL RhB solution (200 mg/L) with a varying mass of WSO-5 from 10 mg to 60 mg for 5 h. The concentration of the remaining RhB in the solution was measured with the aforementioned method.

3. Results and Discussion

3.1. Characterizations

The microstructures and morphologies of WS_2, WSO-5, WSO-30, WSO-60, and WO_3 were characterized by SEM and TEM, and the results are shown in Figures 2 and 3. The SEM images in Figure 2a,b demonstrate that the synthesized WS_2 has a uniform 3D flower-like morphology, which consists of intercrossed nanoflakes with a thickness of several nanometers. According to the thermal-gravimetric analysis (TGA) result (Figure S1), WS_2 starts to lose weight at about 360 °C. Thus, WS_2 microflowers were determined to be calcined at 400 °C for the partial oxidation of WS_2 to WO_3. The obtained WS_2/WO_3 heterostructures were also characterized by SEM (Figure 2c–e). It can be clearly seen that the well-defined flower-like structures crumble gradually with an increase in the calcination time. As displayed in Figure 2c,d, the flower-like microstructures in WSO-5 and WSO-30 are retained, while there is almost no flake morphology in WSO-60. Finally, the three-dimensional structures were entirely destroyed into aggregating particles in WO_3 after the thoroughly oxidation of WS_2 into WO_3 (Figure 2f).
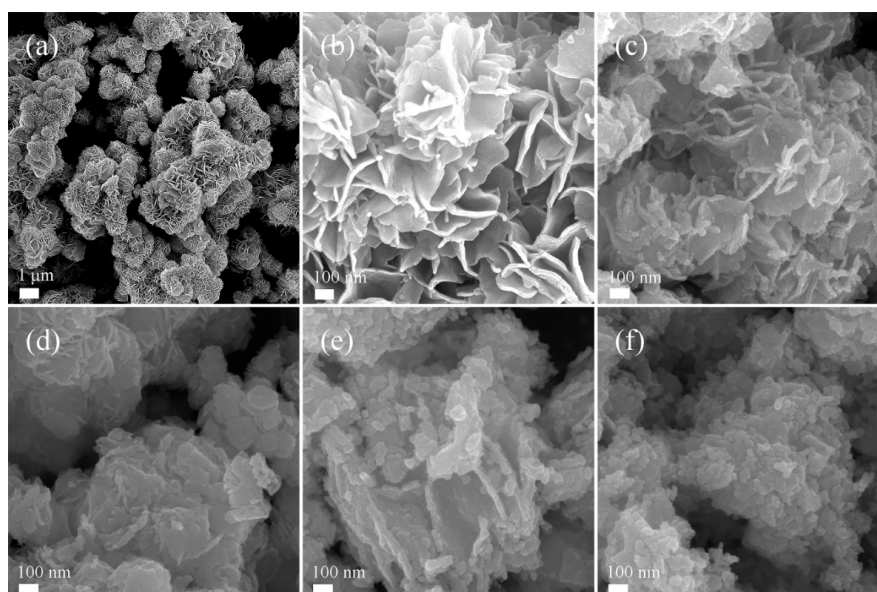

Figure 2. The morphologies of WS_2, WS_2/WO_3, and WO_3. (**a,b**) SEM images of WS_2; (**c–e**) SEM images of WSO-5, WSO-30, and WSO-60, respectively; (**f**) SEM image of WO_3.
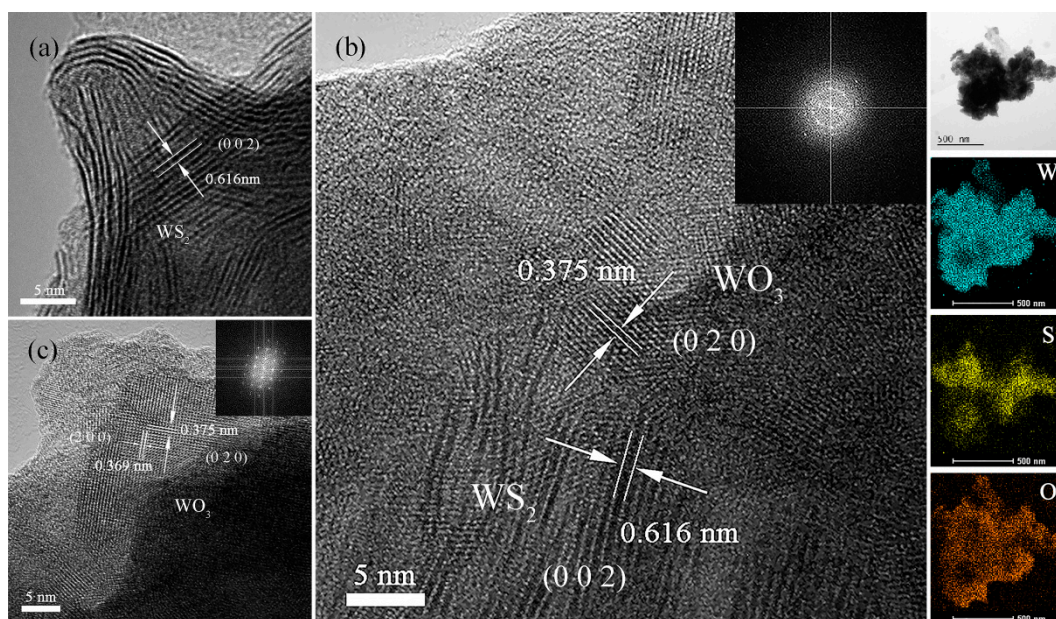
Figure 3. High-resolution TEM (HRTEM) images of (**a**) WS$_2$, (**b**) WSO-5, (**c**) WO$_3$, and (**b** inset) elemental mapping of WSO-5.

The microscopic structures of the obtained composites were further investigated using high-resolution transmission electron microscopy (HRTEM), and the results are displayed in Figure 3. Initially, the interlayer spacing of WS$_2$ nanosheets displayed in the Figure 3a, measured to be 0.616 nm, can be ascribed to the (0 0 2) plane of WS$_2$ [28]. For the sample with a short partial oxidation time of 5 min, a new lattice fringe with d = 0.375 nm appears beside the interlayer spacing of 0.616 nm according to Figure 3b, ascribed to the characteristic interplane distance of the (020) crystallographic plane of WO$_3$. The elemental mapping results of WSO-5 further confirm the uniform distribution of W, S, and O elements on the nanoflakes, suggesting that the WS$_2$ and WO$_3$ species are interconnected on the nanoscale rather than isolated from each other (Figure 3b inset). These polycrystalline structures are also confirmed by a Fast Fourier Transform (FFT) pattern in Figure 3b. Finally, the lattice fringes of WS$_2$ disappear, and only the lattice fringes of WO$_3$ remain (Figure 3c) when the composites are entirely transformed into WO$_3$ particles.

The crystalline information is demonstrated by XRD patterns (Figure 4). From the pattern of pure WS$_2$, several broad peaks at 14.5°, 32.7°, 33.6°, 39.5°, and 58.4° are in good agreement with the (002), (100), (101), (103), and (110) planes of the hexagonal phase of WS$_2$ (JCPDS Card No.08-0237) [29]. With the increase of the calcining time, the intensity of the (0 0 2) peak decreases gradually from WSO-5 to WOS-60. Simultaneously, the peaks at about 24.0° and 33.6°, which are ascribed to the (0 2 0) and (2 2 0) peaks of WO$_3$, emerge and get strengthened. This phenomenon also suggests the successful construction of WS$_2$/WO$_3$ heterostructures. Moreover, pure WO$_3$ was also analyzed, and it was found that WO$_3$ possesses characteristic peaks at 23.1°, 23.8°, 24.1°, 33.6°, and 34.0°, corresponding to the crystal facets (001), (020), (200), (201), and (220) of WO$_3$ (JCPDS Card No.20-1324) respectively [30].
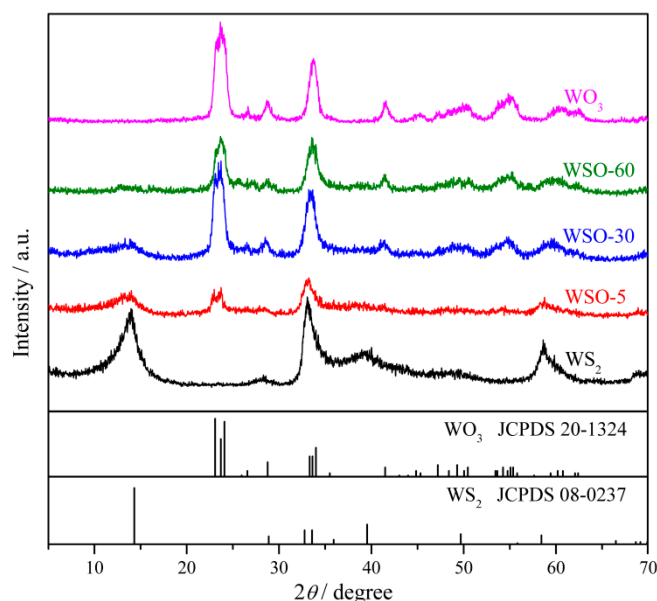
Figure 4. The PXRD patterns of different materials WS_2/WO_3, WS_2, and WO_3.

For the purpose of examining the chemical compositions and electronic states of elements of WSO-n, X-ray photoelectron spectroscopy (XPS) was further utilized in this work. It can be seen from the XPS full-range spectra (Figure 5a) that these obtained composites exhibit characteristic peaks of C, W, O, and S elements. The characteristic peak of C 1s situated at ~284.8 eV, ascribed to the contaminant carbon, was utilized to calibrate the XPS spectra. After the calibration, the corresponding narrow-range W 4f, S 2p, and O 1s spectra were discussed in detail. Figure 5b shows that the O 1s spectra of the WS_2/WO_3 heterostructures can be well fitted into two peaks at 530.94 eV and 531.94 eV, attributed to the O in WO_3 and chemisorbed oxygen-containing materials, respectively [31,32]. As shown in Figure 5c, the two peaks of W 4f5/2 and W 4f7/2 of WS_2 are situated at about 34.60 eV and 33.24 eV. After partial oxidation, new peaks at 37.99 eV and 35.96 eV appeared, which could be assigned to W 4f5/2 and W 4f7/2 in WO_3 [33]. The characteristic peaks of both WS_2 and WO_3 can be clearly observed in WSO-n, which further confirms the successful synthesis of the aimed heterostructures. Ultimately, the S 2p spectra of these composites were characterized (Figure 5d). There are two binding energy of S 2p located at 162.30 eV and 163.70 eV, which can be assigned to the presence of S^{2-} in WS_2. The special peak present at 169.10 eV could be attributed to S^{6+} due to the oxidation of divalent sulfide ions [34]. Significantly, it only existed in WS_2/WO_3 hybrids. The characteristic peaks of S decreased gradually with the oxidation process due to the enhanced transformation from WS_2 to WO_3. Overall, all the XPS spectra results mentioned above demonstrated a successful construction of WS_2/WO_3 heterostructures.
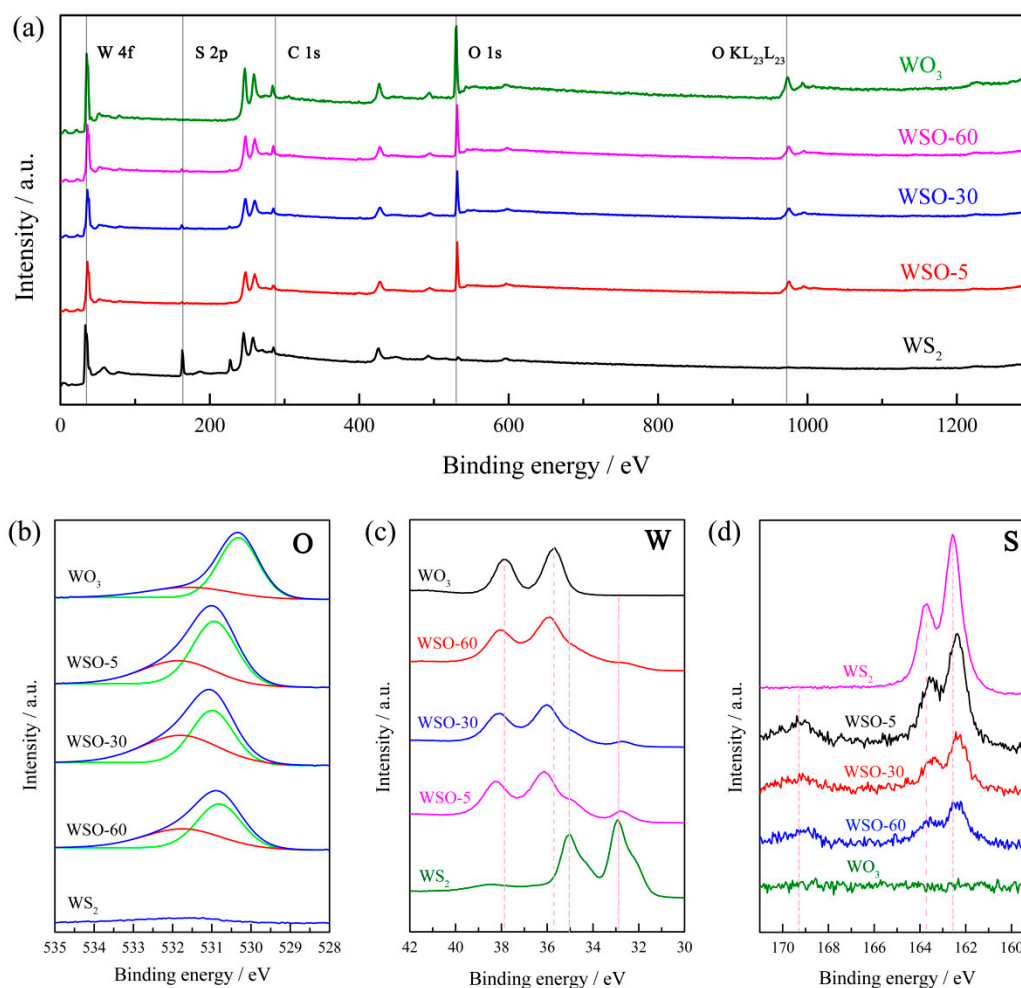
Figure 5. XPS spectra for WS_2, WS_2/WO_3, and WO_3. (**a**) Full-range XPS spectra, (**b**) O 1s spectra, (**c**) W 4f spectra, and (**d**) S 2p spectra.

A contact angle analysis was adopted to assess the obtained materials' wettability, which is traditionally determined by the substrates' morphologies and chemical compositions [35,36]. Initially, the contact angle of pure WS_2 was measured to be about 102° (Figure 6a). After oxidization, a sharp decrement of the contact angle values was observed with all values lower than 20° (Figure 6b–e), indicating the hydrophilicity of WS_2/WO_3 hybrids, and WO_3 was dramatically promoted with the introduction of oxygen atoms. The increasing wettability might result from the formation of hydrogen bonds which are introduced by strong-polar oxygen atoms interacting with water molecules [37,38]. In addition, the high–magnification SEM images of WS_2/WO_3 hybrids (Figure 2c–e) shows that these heterostructures have rougher surface morphologies with voids and many highly water-permeable channels, which can further enhance the hydrophilicity.
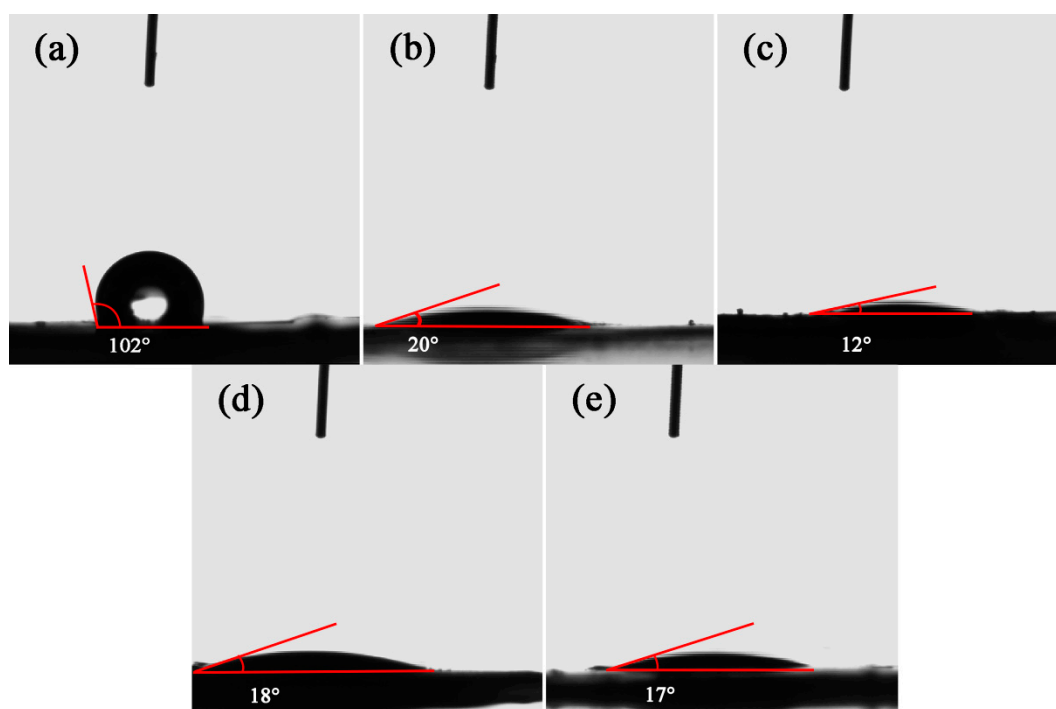
Figure 6. Water Contact angles of (**a**) WS$_2$, (**b**) WSO-5, (**c**) WSO-30, (**d**) WSO-60, and (**e**) WO$_3$.

3.2. Adsorption Knetics

To explore the adsorption kinetics of these newly developed materials on RhB, the effect of the adsorption capacity over contact time was evaluated. As shown in Figure 7a, all the WS$_2$/WO$_3$ hybrid samples exhibited similar trends, with the sorption capacities increasing rapidly during the first 100 min, then gradually reaching equilibrium with a further increase of the adsorption time. Obviously, the pure WS$_2$ showed a poor adsorption capacity of merely 16.4 mg/g, which can be ascribed to the hydrophobic surface property. After the introduction of oxygen atoms with a short duration time of 5 min, the adsorption capacity got a tremendous promotion (237.1 mg/g) due to the stronger hydrophilicity, as well as to the retention of the superior properties of WS$_2$. However, with the further increment of the oxidation duration, the adsorption capacity gradually declined until reaching pure WO$_3$, which exhibited a low adsorption performance of 30.1 mg/g.

Three empirical kinetic models were adopted to conduct a further analysis toward the adsorption kinetics, namely, a pseudo-first-order model (Equation (3)), pseudo-second order model (Equation (4)), and Weber-Morris model (Equation (5)):

$$\ln(Q_e - Q_t) = \ln Q_e - k_1 t, \tag{3}$$

$$\frac{t}{Q_t} = \frac{1}{k_2 Q_e^2} + \frac{t}{Q_e}, \tag{4}$$

$$Q_t = k_i t^{1/2} + c, \tag{5}$$

where Q_e (mg/g) and Q_t (mg/g) represent the adsorption capacities of RhB onto samples at equilibrium and time t (min); c (mg/g) is a constant; k_1 (min^{-1}), k_2 (g·mg^{-1}·min^{-1}), and k_i (mg·g^{-1}·min$^{-1/2}$) are the rate constants of the pseudo-first order, pseudo-second order, and Weber-Morris models, respectively.

The fitting results are displayed in Figure 7b–d, and the calculated kinetic parameters are summarized in Table S1. Compared with the pseudo-first-order model and Weber-Morris model, the pseudo-second-order model exhibits better correlation results for the experimental data, with a higher R^2 value (above 0.99).
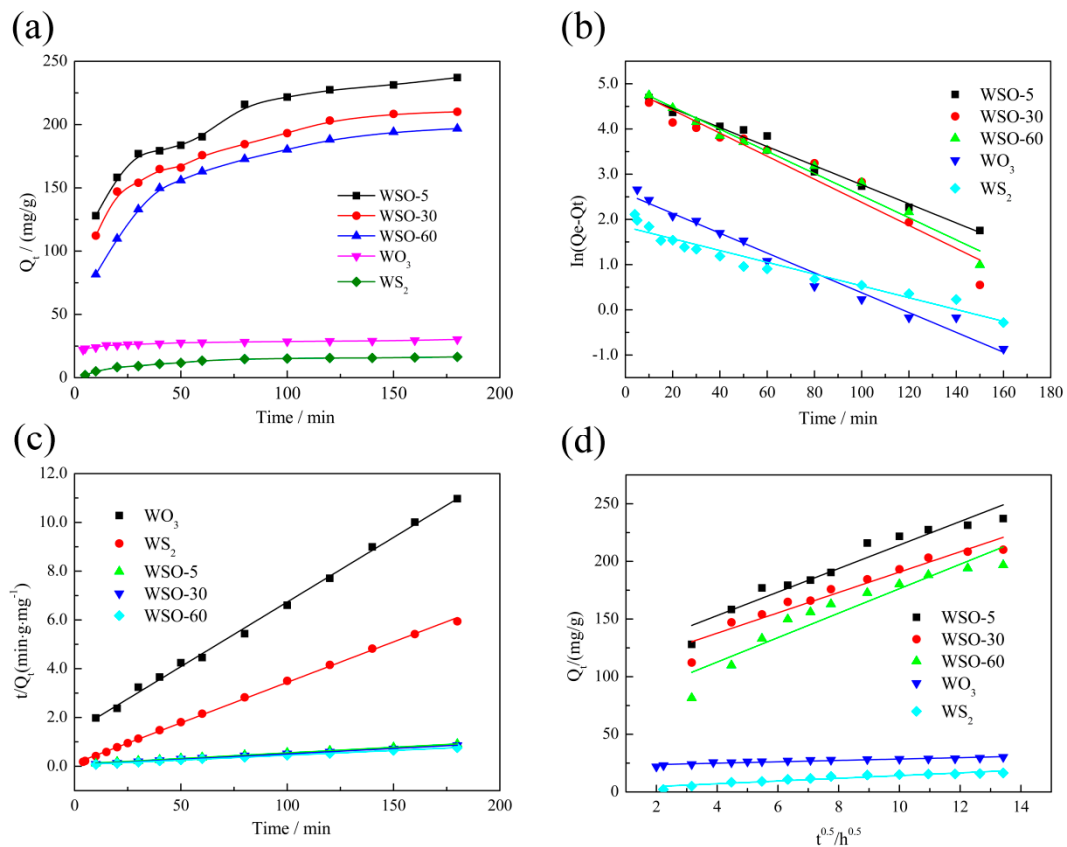
Figure 7. (**a**) The effect of the contact time on the adsorption capacity of WS$_2$, WS$_2$/WO$_3$, and WO$_3$ for RhB; the fitted kinetic data with (**b**) the pseudo-first-order model, (**c**) pseudo-second-order model, and (**d**) Weber-Morris model.

3.3. Adsorption Isotherms

To elucidate the equilibrium states of RhB dye molecules on materials and in liquid surroundings, the adsorption isotherms were conducted [39]. In particular, WSO-5 was chosen as the model material due to its higher adsorption capacity. The adsorption isotherms of RhB on WSO-5 were carried out at gradient temperatures of 30, 40 and 50 °C. As shown in Figure 8, the adsorption isotherms exhibited conventional L-types with obvious platforms. The results showed that the increasing temperature in circumstance could facilitate the adsorption for WSO-5, suggesting an endothermic adsorption process. Furthermore, a straightforward statistical physics model was utilized to fit the adsorption isotherms of RhB. The mathematical equation of the model is presented as follows [40]:

$$Q_e = \frac{nD_m}{1 + \left(\frac{c_{1/2}}{c_e}\right)^n},\qquad(6)$$

where *n* represents the number of RhB molecules per site of adsorbent, D_m (mg/g) is the density of the receptor sites, and $c_{1/2}$ (mg/L) means the concentration at half saturation of the formed layer. According to the statistic physics model, the adsorption capacity at saturation Q_{sat} is given by [41]:

$$Q_{sat} = nD_m.\qquad(7)$$

The expression of the adsorption energy *E*, which contains the solubility c_s (mg/L) of the adsorbates, can be expressed as follows [41,42]:

$$E = RTln(c_s/c_{1/2}).\qquad(8)$$

The fitted model parameters were determined through nonlinear regressions of the experimental sorption isotherms (Table 1). The values of R^2 are close to unity, indicating that this monolayer model could be used to elucidate the sorption mechanisms of the test adsorbents.
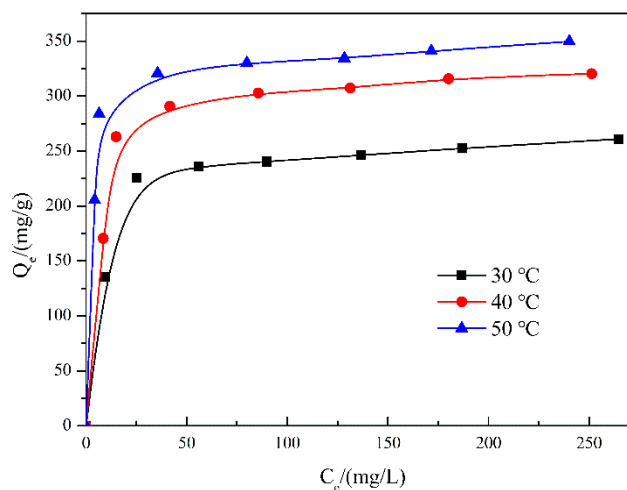
Figure 8. The adsorption isotherms of RhB on WSO-5 at pH 6. (30, 40 and 50 °C).

**Table 1.** The parameters of the monolayer adsorption model under different tested temperatures.

T (°C)	n	D_m (mg/g)	Q_{sat} (mg/g)	E (kJ/mol)	R^2
30	1.840	136.3	250.8	5.901	0.9993
40	2.495	123.9	309.1	6.336	0.9992
50	2.922	114.8	335.4	8.575	0.9993

The parameter n gives information about the orientation states of the adsorbates on the adsorbent surface. Traditionally, two situations are taken into consideration: if $n < 1$, the adsorbates would interact with the multifunctional groups of adsorbents (horizontal orientation); if $n \geq 1$, more than one adsorbate molecules would be anchored in one receptor site on the adsorbent surface (non-horizontal orientation) [43]. The effects of the temperature on this parameter, displayed in Figure 9a, show that the values of n in all tested temperature are above unity, varying from 1.84 to 2.92. In consequence, this evidence implies a multi-molecular adsorption process of RhB molecules with an oblique orientation on WS_2/WO_3 [40].

Moreover, the effect of the temperature on the receptor sites' density D_m was also interpreted, and the results are shown in Figure 9b. This decreasing tendency is related to the increasing number of molecules captured per site, leading to a tendency of aggregation which would hinder the accessibility of the RhB molecules to the adsorption receptor sites [42,44].

The correlation of the parameters (n and D_m) of the monolayer can be examined by the variation of the adsorption capacity on the temperature. As shown in Figure 9c, the effect of the temperature on the parameter Q_{sat} indicates that the increment of temperature results in an increasing Q_{sat} value, which further verifies an endothermic process of RhB adsorption.

The adsorption energy E was calculated to further clarify the interactions between the RhB molecules and the adsorbent surface. The E values were calculated via Equation (8), and the results that E evolve with the tested temperature are displayed in Figure 9d. The results confirm again that the adsorption is an endothermic process, which matches the analysis conclusion of Q_{sat} well. Furthermore, the results show that the adsorption is a physisorption process within the investigated temperatures, since all E values are lower than 10 kJ/mol [42].
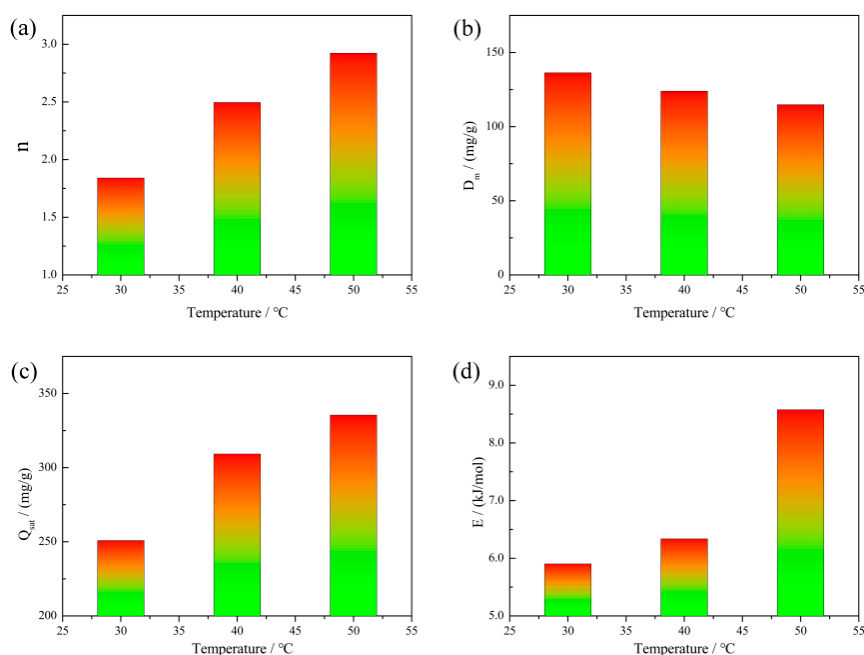
Figure 9. (**a**) The effect of the temperature on the number of molecules per site, (**b**) the density of receptor sites, (**c**) the adsorption capacity at saturation, and (**d**) the adsorption energy of WSO-5.

3.4. Effect of Adsorbent Dosage and Solution pH

3.4.1. Effect of Adsorbent Dosage

The cost of an adsorbent in practical application depends, to a large extent, on its specific dosage to achieve the wastewater treatment standards. In this work, the correlation of the adsorbent dosage and the removal efficiency of RhB was explored (Figure 10). It can be clearly observed in Figure 10a that the removal efficiency of RhB increases from about 24% to almost 95% as the dosage increases from 0.125 to 1.5 g/L. However, there is no evident growth anymore when the dosage exceeds 1.0 g/L. The reason for this might be that more available binding sites are provided to capture RhB molecules in solution with the increased content of WS_2/WO_3 composites. To reduce the expense of sewage disposal, an optimal WS_2/WO_3 dosage of 1 g/L is suggested for the efficient elimination of RhB, with an initial concentration of 200 mg/L at pH 6.0.
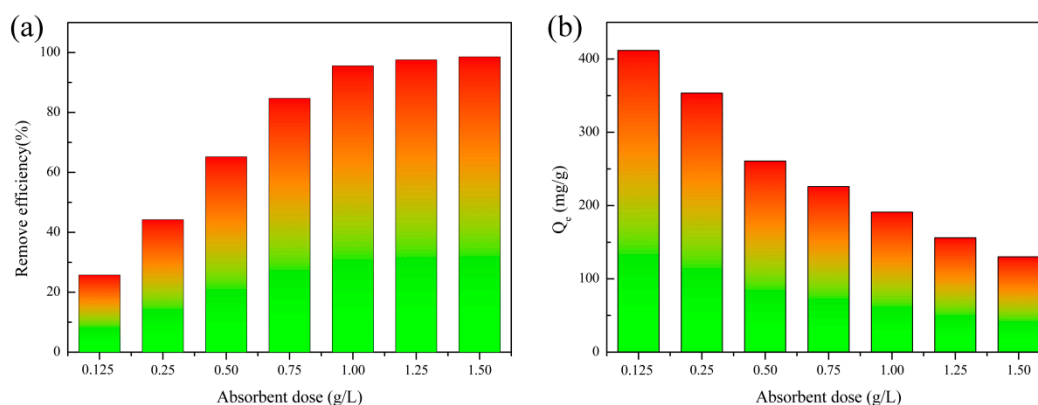

Figure 10. (**a**) The adsorption percentage and (**b**) adsorption amount of RhB on WS_2/WO_3 as a function of the adsorbent content at 30 °C, pH 6.0, and $C_{initial}$ 200 mg/L.

Meanwhile, the mass-based adsorption amount of RhB dye gradually decreased with the increment of solid content (Figure 10b). This can be explained by the fact that WS_2/WO_3 microflowers dispersed

well in solution and that the surface active sites were highly available to form a stable complex with RhB molecules at low dosages. However, higher solid dosages would cause the collision and aggregation of the WS$_2$/WO$_3$ adsorbent, resulting in a decrease in the density of the active sites. In addition, under a vigorous stirring rate (200 rpm), the inter-collision between WS2/WO3 at a higher solid content would also cause the desorption of some weak-linked RhB molecules and ultimately reduce the adsorption amount [22,45].

3.4.2. Effect of Solution pH

Usually, the solution pH is a significant factor that exerts great influence on the adsorption of dyes onto the adsorbents. Therefore, the effect of the pH on RhB adsorption for the WS$_2$/WO$_3$ hybrid was investigated, and the results are exhibited in Figure 11a. The equilibrium adsorption amount Q_e (mg/g) exhibited an increasing trend when raising pH values from 2 to 6 and then sharply decreased when the initial pH values exceeded 7. This trend suggests that WS$_2$/WO$_3$ exhibits an excellent performance for RhB adsorption under neutral or slightly acidic circumstances, which can be interpreted by the correspondingly extraordinary negative Zeta potentials of the WS$_2$/WO$_3$ materials displayed in this pH range (pH ≥ 4) (Figure 11b) that facilitate the attraction of RhB dye molecules.
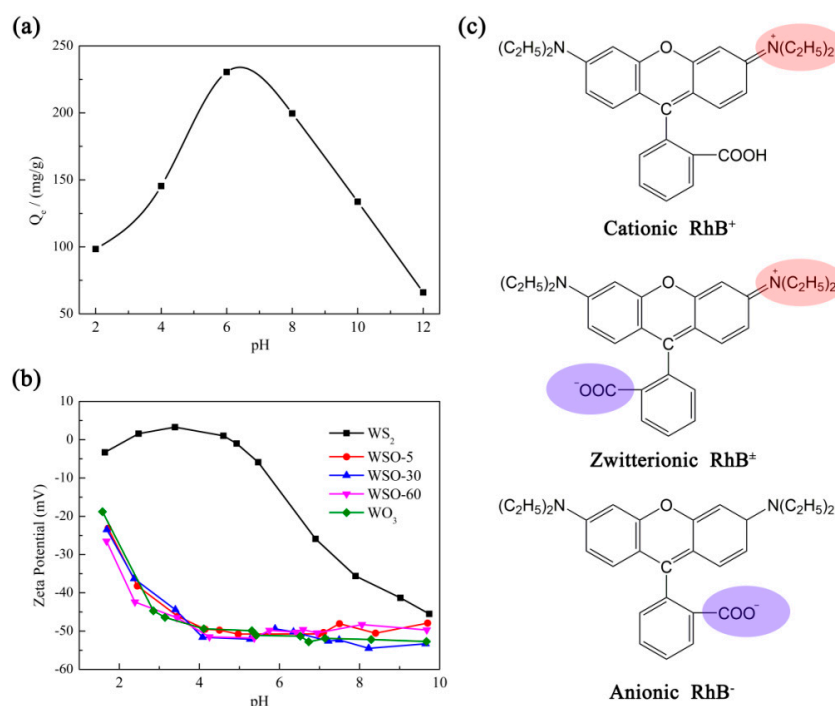

Figure 11. (**a**) The effect of the pH on the adsorption of RhB on WSO-5. (Adsorbent = 20 mg, RhB = 40 mL of 200 mg/L, T = 30 °C.) (**b**) The Zeta potential of WS$_2$, WS$_2$/WO$_3$ hybrids, and WO$_3$ at various pH values. (**c**) The molecular structures of RhB in its zwitterionic, cationic, and anionic form, respectively.

The interrelation of the existing forms of RhB in solution and the adsorption capacity were further studied. It has been reported that RhB molecules exist in three forms in solution, including the cationic, anionic, and zwitterionic forms (Figure 11c) [46]. In an acidic environment, the RhB molecule is ionized and exists predominantly in its cationic form (RhB$^+$). However, the competitive protons introduced by the acidic environment exert a positive charge effect on the WS$_2$/WO$_3$ surface, which is reflected by the Zeta potential analysis (Figure 11b). Therefore, under these circumstances it is difficult for WS$_2$/WO$_3$ to come into contact with RhB$^+$ molecules, owing to the electrostatic repulsion. With gradually increased pH values, the fraction of the cationic form (RhB$^+$) decreased, while the zwitterionic form (RhB$^±$) increased simultaneously. These zwitterionic RhB molecules, with

both C=N$^+$ and COO$^-$ groups, would aggregate on the active sites, resulting in a higher adsorption capacity [47,48]. When the pH rose up to a higher value above 7, the anionic form (RhB$^-$) increased, and the adsorption capacity of WS$_2$/WO$_3$ significantly decreased owing to the electrostatic repulsion between negatively charged RhB$^-$ and negative WS$_2$/WO$_3$.

3.5. Adsorption Mechanism

The adsorption mechanism of RhB dye onto WS$_2$/WO$_3$ heterostructures was further elucidated by considering all the results discussed above. As shown in Figure 12a, the electronegative sulfur and oxygen atoms in the polar active sites of the WS$_2$/WO$_3$ heterostructures would connect with the RhB$^\pm$ molecules by electrostatic attraction, subsequently inducing the adsorption process. According to the fitting results of the monolayer model mentioned before, RhB$^\pm$ molecules exhibit a non-horizontal orientation on the WS$_2$/WO$_3$ surface. Specifically, this is primarily conducted via the RhB$^\pm$ molecules aggregating layer-by-layer on the active sites in a head-to-tail way, since this zwitterionic form has positive and negative sites simultaneously [22]. The adsorption of RhB molecules onto materials can be detected through a comparison of the FTIR spectroscopy before and after adsorption toward RhB (Figure 12b). The peak at about 580 cm^{-1} in the spectra of WS$_2$/WO$_3$ is assigned to O–W–O vibration. Meanwhile, the new peaks at about 1590 and 1340 cm^{-1} belonging to the characteristic peaks of in-ring C–C and C–H stretching vibrations in the aromatic ring of the RhB molecule could be detected after the adsorption of dye (Figure 12c) [26,49]. However, there are no obvious dye characteristic peaks in the spectra of WS$_2$ and WO$_3$, which indicates that few RhB molecules are adsorbed onto these two materials. Besides, no characteristic peaks of RhB were observed after the desorption process, which means that electrostatic attraction is responsible for the RhB adsorption by WS$_2$/WO$_3$. On the other hand, the XRD patterns in Figure 12d also prove that the adsorption process didn't change the crystal structure of WSO-5. The characteristic peaks are well retained after adsorption, and there are no obvious peaks shifts, which demonstrates that the adsorption is a complete physical behavior that occurs primarily through electrostatic attraction.
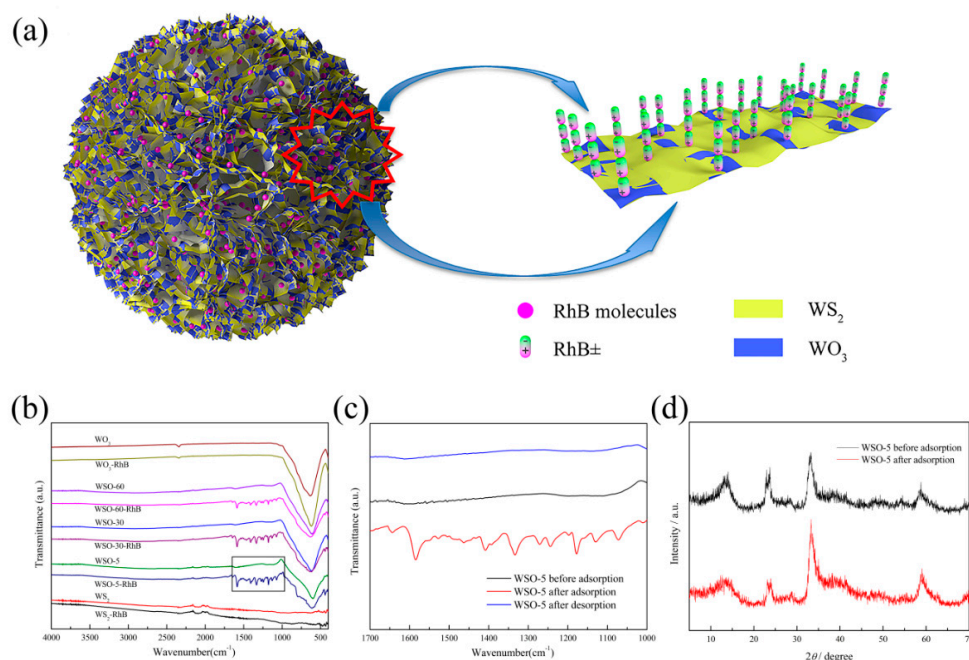
Figure 12. (**a**) The adsorption mechanism of WSO-5 microflowers toward RhB; (**b**) the FTIR spectra of WS$_2$, WS$_2$/WO$_3$, and WO$_3$ before and after the adsorption of RhB dye; (**c**) The enlarged image of WSO-5 of the zone marked in (**b**); and (**d**) the XRD patterns of WSO-5 before and after the adsorption of RhB dye.

3.6. Recyclability

For the practical application of an adsorbent, a quick adsorption rate and high adsorption capacity are of great significance, and the reusability of the adsorbent should be taken into consideration as well. After the adsorption experiments, the adsorbent was washed with ethanol as the eluting agent and reused for the next adsorption process. According to Figure 13, the adsorption performance of WSO-5 toward RhB dye slightly decreased after the first cycle, while remaining almost constant in the following cycles. These results demonstrate that WS_2/WO_3 has a good stability and can be regenerated and reused efficiently for the treatment of waste water contaminated with RhB dye.
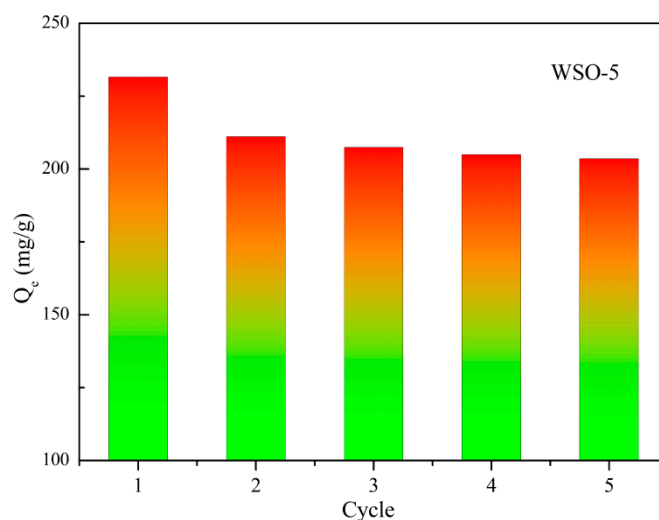

Figure 13. The recyclability of WSO-5.

3.7. Comparison with Other Adsorption Materials

To sum up, in this study the WS_2/WO_3 hybrids were first synthesized and utilized to investigate their dye adsorption performance. The comparison of the mass-based adsorption performance between them and some other reported TMD absorbents is presented in Table 2. It can be clearly seen that the WS_2/WO_3 hybrids, particularly WSO-5, exhibit a higher adsorption capacity and relatively medium adsorption time. Because of the multiple advantages, such as a simple synthesis process, high removal efficiency, and good reusability, the WS_2/WO_3 heterostructure could be a promising candidate for the elimination and separation of organic dyes from wastewater.

Table 2. A comparison of the adsorption performance of the WS_2, WO_3, and WS_2/WO_3 heterostructures with other reported TMD adsorbents.

Adsorbents	Dyes	Adsorption Capacity (mg/g)	Adsorption Time (min)	References
MoS_2 nanosheets	RhB	163	420	[27]
2D MoS_2 nanosheets	MB	146	5	[50]
Flower-like MoS_2	RhB	55.0	180	[51]
MoS_2-glue sponges	RhB	127	60	[22]
Fe_3O_4/MoS_2	RhB	22.0	30	[52]
Flower-like WS_2	RhB	16.4	100	This work
WO_3 particles	RhB	30.4	100	This work
Flower-like WSO-5	RhB	237	100	This work

4. Discussion

In this work, a new type of WS_2/WO_3 heterostructure, which could be used as excellent absorbents, was developed and fabricated by coupling a solvothermal synthesis method with

a partial oxidation strategy. Different characterization results confirmed the successful fabrication of WS$_2$/WO$_3$ heterostructures, which possess more negative surface charges and which highly promoted hydrophilicity after a partial oxidation. The synthesized heterostructures were employed for the decontamination of dyes, and the results indicate that WSO-5 has an enhanced adsorption capacity of 237.1 mg/g, compared with pure WS$_2$ and WO$_3$, which exhibited a limited capacity of 16.4 and 30.4 mg/g, respectively. Besides, three models were applied to simulate the kinetics in the adsorption process, and the results prove that the pseudo-second-order model gives better fitting results. Furthermore, the adsorption isotherms were also conducted by a precise monolayer adsorption model to reveal the interaction between the adsorbent and adsorbate, demonstrating a non-horizontal orientation of the RhB molecules and an endothermic physisorption process. Finally, the recyclability study showed that WS$_2$/WO$_3$ can be easily regenerated through a simple ethanol washing and that the adsorption performance was well-maintained after five cycles. These results indicate that WS$_2$/WO$_3$ can be a promising adsorbent for the removal of RhB dye from wastewater. Overall, the partial oxidation strategy can introduce more negative surface charges and enhance hydrophilicity, which gives an indication for the surficial modification of other TMD materials and their application in the elimination of dyes.

References

1. Okesola, B.O.; Smith, D.K. Applying low-molecular weight supramolecular gelators in an environmental setting self-assembled gels as smart materials for pollutant removal. *Chem. Soc. Rev.* **2016**, *45*, 4226–4251. [CrossRef]

2. Bi, J.; Huang, X.; Wang, J.; Wang, T.; Wu, H.; Yang, J.; Lu, H.; Hao, H. Oil-phase cyclic magnetic adsorption to synthesize Fe$_3$O$_4$@C@TiO$_2$-nanotube composites for simultaneous removal of Pb(II) and Rhodamine B. *Chem. Eng. J.* **2019**, *366*, 50–61. [CrossRef]

3. Tan, K.B.; Vakili, M.; Horri, B.A.; Poh, P.E.; Abdullah, A.Z.; Salamatinia, B. Adsorption of dyes by nanomaterials: Recent developments and adsorption mechanisms. *Sep. Purif. Technol.* **2015**, *150*, 229–242. [CrossRef]

4. Chen, J.; Pu, Y.; Wang, C.; Han, J.; Zhong, Y.; Liu, K. Synthesis of a novel nanosilica-supported poly β-cyclodextrin sorbent and its properties for the removal of dyes from aqueous solution. *Colloids Surf. A* **2018**, *538*, 808–817. [CrossRef]

5. Zhang, J.; Yan, X.; Hu, X.; Feng, R.; Zhou, M. Direct carbonization of Zn/Co zeolitic imidazolate frameworks for efficient adsorption of Rhodamine B. *Chem. Eng. J.* **2018**, *347*, 640–647. [CrossRef]

6. Wen, T.; Wang, J.; Yu, S.; Chen, Z.; Hayat, T.; Wang, X. Magnetic Porous Carbonaceous Material Produced from Tea Waste for Efficient Removal of As(V), Cr(VI), Humic Acid, and Dyes. *ACS Sustain. Chem. Eng.* **2017**, *5*, 4371–4380. [CrossRef]

7. Lu, H.; Wang, J.; Li, F.; Huang, X.; Tian, B.; Hao, H. Highly Efficient and Reusable Montmorillonite/Fe$_3$O$_4$/Humic Acid Nanocomposites for Simultaneous Removal of Cr(VI) and Aniline. *Nanomaterials* **2018**, *8*, 537. [CrossRef]

8. Huang, X.; Yang, J.; Wang, J.; Bi, J.; Xie, C.; Hao, H. Design and synthesis of core–shell Fe_3O_4@PTMT composite magnetic microspheres for adsorption of heavy metals from high salinity wastewater. *Chemosphere* **2018**, *206*, 513–521. [CrossRef]

9. Du, X.; Zhang, H.; Hao, X.; Guan, G.; Abudula, A. Facile Preparation of Ion-Imprinted Composite Film for Selective Electrochemical Removal of Nickel(II) Ions. *ACS Appl. Mater. Interfaces* **2014**, *6*, 9543–9549. [CrossRef]

10. Körbahti, B.K.; Artut, K.; Geçgel, C.; Özer, A. Electrochemical decolorization of textile dyes and removal of metal ions from textile dye and metal ion binary mixtures. *Chem. Eng. J.* **2011**, *173*, 677–688. [CrossRef]

11. Chen, X.; Mao, S.S. Titanium Dioxide Nanomaterials: Synthesis, Properties, Modifications, and Applications. *Chem. Rev.* **2007**, *107*, 2891–2959. [CrossRef] [PubMed]

12. Li, B.; Dong, Y.; Zou, C.; Xu, Y. Iron(III)–Alginate Fiber Complex as a Highly Effective and Stable Heterogeneous Fenton Photocatalyst for Mineralization of Organic Dye. *Ind. Eng. Chem. Res.* **2014**, *53*, 4199–4206. [CrossRef]

13. Yadav, A.; Mukherji, S.; Garg, A. Removal of Chemical Oxygen Demand and Color from Simulated Textile Wastewater Using a Combination of Chemical/Physicochemical Processes. *Ind. Eng. Chem. Res.* **2013**, *52*, 10063–10071. [CrossRef]

14. Luo, L.; Wang, Y.; Zhu, M.; Cheng, X.; Zhang, X.; Meng, X.; Huang, X.; Hao, H. Co–Cu–Al Layered Double Oxides as Heterogeneous Catalyst for Enhanced Degradation of Organic Pollutants in Wastewater by Activating Peroxymonosulfate: Performance and Synergistic Effect. *Ind. Eng. Chem. Res.* **2019**, *58*, 8699–8711. [CrossRef]

15. Thung, W.-E.; Ong, S.-A.; Ho, L.-N.; Wong, Y.-S.; Ridwan, F.; Lehl, H.K.; Oon, Y.-L.; Oon, Y.-S. Biodegradation of Acid Orange 7 in a combined anaerobic-aerobic up-flow membrane-less microbial fuel cell: Mechanism of biodegradation and electron transfer. *Chem. Eng. J.* **2018**, *336*, 397–405. [CrossRef]

16. Ren, X.; Chen, C.; Nagatsu, M.; Wang, X. Carbon nanotubes as adsorbents in environmental pollution management: A review. *Chem. Eng. J.* **2011**, *170*, 395–410. [CrossRef]

17. Chen, C.; Wang, X. Adsorption of Ni(II) from Aqueous Solution Using Oxidized Multiwall Carbon Nanotubes. *Ind. Eng. Chem. Res.* **2006**, *45*, 9144–9149. [CrossRef]

18. Shen, T.; Luo, J.; Zhang, S.; Luo, X. Hierarchically mesostructured MIL-101 metal–organic frameworks with different mineralizing agents for adsorptive removal of methyl orange and methylene blue from aqueous solution. *J. Environ. Chem. Eng.* **2015**, *3*, 1372–1383. [CrossRef]

19. Chen, C.; Chen, D.; Xie, S.; Quan, H.; Luo, X.; Guo, L. Adsorption Behaviors of Organic Micropollutants on Zirconium Metal–Organic Framework UiO-66: Analysis of Surface Interactions. *ACS Appl. Mater. Interfaces* **2017**, *9*, 41043–41054. [CrossRef]

20. Zhao, G.; Li, J.; Ren, X.; Chen, C.; Wang, X. Few-Layered Graphene Oxide Nanosheets As Superior Sorbents for Heavy Metal Ion Pollution Management. *Environ. Sci. Technol.* **2011**, *45*, 10454–10462. [CrossRef]

21. Jiang, D.B.; Jing, C.; Yuan, Y.; Feng, L.; Liu, X.; Dong, F.; Dong, B.; Zhang, Y.X. 2D-2D growth of NiFe LDH nanoflakes on montmorillonite for cationic and anionic dye adsorption performance. *J. Colloid. Interface Sci.* **2019**, *540*, 398–409. [CrossRef] [PubMed]

22. Fang, Y.; Huang, Q.; Liu, P.; Shi, J.; Xu, G. Easy-separative MoS_2-glue sponges with high-efficient dye adsorption and excellent reusability for convenient water treatment. *Colloids Surf. A* **2018**, *540*, 112–122. [CrossRef]

23. Huang, Q.; Fang, Y.; Shi, J.; Liang, Y.; Zhu, Y.; Xu, G. Flower-Like Molybdenum Disulfide for Polarity-Triggered Accumulation/Release of Small Molecules. *ACS Appl. Mater. Interfaces* **2017**, *9*, 36431–36437. [CrossRef] [PubMed]

24. Wu, J.M.; Chang, W.E.; Chang, Y.T.; Chang, C.-K. Piezo-Catalytic Effect on the Enhancement of the Ultra-High Degradation Activity in the Dark by Single- and Few-Layers MoS_2 Nanoflowers. *Adv. Mater.* **2016**, *28*, 3718–3725. [CrossRef]

25. Zhang, L.; Wu, H.B.; Yan, Y.; Wang, X.; Lou, X.W. Hierarchical MoS_2 microboxes constructed by nanosheets with enhanced electrochemical properties for lithium storage and water splitting. *Energy Environ. Sci.* **2014**, *7*, 3302–3306. [CrossRef]

26. Wang, X.; Ding, J.; Yao, S.; Wu, X.; Feng, Q.; Wang, Z.; Geng, B. High supercapacitor and adsorption behaviors of flower-like MoS_2 nanostructures. *J. Mater. Chem. A* **2014**, *2*, 15958–15963. [CrossRef]

27. Li, H.; Xie, F.; Li, W.; Fahlman, B.D.; Chen, M.; Li, W. Preparation and adsorption capacity of porous MoS_2 nanosheets. *RSC Adv.* **2016**, *6*, 105222–105230. [CrossRef]

28. Yan, H.; Li, J.; Liu, D.; Jing, X.; Wang, D.; Meng, L. Controlled preparation of high quality WS$_2$ nanostructures by a microwave-assisted solvothermal method. *Crystengcomm* **2018**, *20*, 2324–2330. [CrossRef]

29. Wu, Z.; Fang, B.; Bonakdarpour, A.; Sun, A.; Wilkinson, D.P.; Wang, D. WS$_2$ nanosheets as a highly efficient electrocatalyst for hydrogen evolution reaction. *Appl. Catal. B Environ.* **2012**, *125*, 59–66. [CrossRef]

30. Chen, S.; Hu, Y.; Meng, S.; Fu, X. Study on the separation mechanisms of photogenerated electrons and holes for composite photocatalysts g-C$_3$N$_4$-WO$_3$. *Appl. Catal. B Environ.* **2014**, *150–151*, 564–573. [CrossRef]

31. Zhao, X.; Feng, J.; Liu, J.; Lu, J.; Shi, W.; Yang, G.; Wang, G.; Feng, P.; Cheng, P. Metal–Organic Framework-Derived ZnO/ZnS Heteronanostructures for Efficient Visible-Light-Driven Photocatalytic Hydrogen Production. *Adv. Sci.* **2018**, *5*, 1700590. [CrossRef] [PubMed]

32. Shpak, A.P.; Korduban, A.M.; Medvedskij, M.M.; Kandyba, V.O. XPS studies of active elements surface of gas sensors based on WO$_{3-x}$ nanoparticles. *J. Electron Spectrosc.* **2007**, *156–158*, 172–175. [CrossRef]

33. Chen, T.-Y.; Chang, Y.-H.; Hsu, C.-L.; Wei, K.-H.; Chiang, C.-Y.; Li, L.-J. Comparative study on MoS$_2$ and WS$_2$ for electrocatalytic water splitting. *Int. J. Hydrogen Energy* **2013**, *38*, 12302–12309. [CrossRef]

34. Zhou, P.; Xu, Q.; Li, H.; Wang, Y.; Yan, B.; Zhou, Y.; Chen, J.; Zhang, J.; Wang, K. Fabrication of Two-Dimensional Lateral Heterostructures of WS$_2$/WO$_3$·H$_2$O Through Selective Oxidation of Monolayer WS$_2$. *Angew. Chem. Int. Ed.* **2015**, *54*, 15226–15230. [CrossRef] [PubMed]

35. Zhou, Y.; Wang, B.; Zhang, X.; Zhao, M.; Li, E.; Yan, H. The modifications of the surface wettability of amorphous carbon films. *Colloids Surf. A* **2009**, *335*, 128–132. [CrossRef]

36. Webb, H.K.; Crawford, R.J.; Ivanova, E.P. Wettability of natural superhydrophobic surfaces. *Adv. Colloid Interface Sci.* **2014**, *210*, 58–64. [CrossRef]

37. Wang, J.; Hu, J.; Wen, Y.; Song, Y.; Jiang, L. Hydrogen-Bonding-Driven Wettability Change of Colloidal Crystal Films: From Superhydrophobicity to Superhydrophilicity. *Chem. Mater.* **2006**, *18*, 4984–4986. [CrossRef]

38. Xin, B.; Hao, J. Reversibly switchable wettability. *Chem. Soc. Rev.* **2010**, *39*, 769–782. [CrossRef]

39. Shan, R.-R.; Yan, L.-G.; Yang, K.; Yu, S.-J.; Hao, Y.-F.; Yu, H.-Q.; Du, B. Magnetic Fe$_3$O$_4$/MgAl-LDH composite for effective removal of three red dyes from aqueous solution. *Chem. Eng. J.* **2014**, *252*, 38–46. [CrossRef]

40. Azha, S.F.; Sellaoui, L.; Shamsudin, M.S.; Ismail, S.; Bonilla-Petriciolet, A.; Ben Lamine, A.; Erto, A. Synthesis and characterization of a novel amphoteric adsorbent coating for anionic and cationic dyes adsorption: Experimental investigation and statistical physics modelling. *Chem. Eng. J.* **2018**, *351*, 221–229. [CrossRef]

41. Sellaoui, L.; Soetaredjo, F.E.; Ismadji, S.; Bonilla-Petriciolet, A.; Belver, C.; Bedia, J.; Ben Lamine, A.; Erto, A. Insights on the statistical physics modeling of the adsorption of Cd^{2+} and Pb^{2+} ions on bentonite-chitosan composite in single and binary systems. *Chem. Eng. J.* **2018**, *354*, 569–576. [CrossRef]

42. Sellaoui, L.; Guedidi, H.; Knani, S.; Reinert, L.; Duclaux, L.; Ben Lamine, A. Application of statistical physics formalism to the modeling of adsorption isotherms of ibuprofen on activated carbon. *Fluid Phase Equilib.* **2015**, *387*, 103–110. [CrossRef]

43. Bi, J.; Huang, X.; Wang, J.; Tao, Q.; Lu, H.; Luo, L.; Li, G.; Hao, H. Self-assembly of immobilized titanate films with different layers for heavy metal ions removal from wastewater: Synthesis, modeling and mechanism. *Chem. Eng. J.* **2020**, *380*, 122564. [CrossRef]

44. Li, Z.; Gómez-Avilés, A.; Sellaoui, L.; Bedia, J.; Bonilla-Petriciolet, A.; Belver, C. Adsorption of ibuprofen on organo-sepiolite and on zeolite/sepiolite heterostructure: Synthesis, characterization and statistical physics modeling. *Chem. Eng. J.* **2019**, *371*, 868–875. [CrossRef]

45. Yang, S.; Zong, P.; Hu, J.; Sheng, G.; Wang, Q.; Wang, X. Fabrication of β-cyclodextrin conjugated magnetic HNT/iron oxide composite for high-efficient decontamination of U(VI). *Chem. Eng. J.* **2013**, *214*, 376–385. [CrossRef]

46. Wang, J.; Gao, M.; Shen, T.; Yu, M.; Xiang, Y.; Liu, J. Insights into the efficient adsorption of rhodamine B on tunable organo-vermiculites. *J. Hazard. Mater.* **2019**, *366*, 501–511. [CrossRef]

47. Anandkumar, J.; Mandal, B. Adsorption of chromium(VI) and Rhodamine B by surface modified tannery waste: Kinetic, mechanistic and thermodynamic studies. *J. Hazard. Mater.* **2011**, *186*, 1088–1096. [CrossRef]

48. Gao, Y.; Wang, Y.; Zhang, H. Removal of Rhodamine B with Fe-supported bentonite as heterogeneous photo-Fenton catalyst under visible irradiation. *Appl. Catal. B Environ.* **2015**, *178*, 29–36. [CrossRef]

49. Sang, Y.; Zhao, Z.; Zhao, M.; Hao, P.; Leng, Y.; Liu, H. From UV to Near-Infrared, WS$_2$ Nanosheet: A Novel Photocatalyst for Full Solar Light Spectrum Photodegradation. *Adv. Mater.* **2015**, *27*, 363–369. [CrossRef]

50. Qiao, X.-Q.; Hu, F.-C.; Tian, F.-Y.; Hou, D.-F.; Li, D.-S. Equilibrium and kinetic studies on MB adsorption by ultrathin 2D MoS$_2$ nanosheets. *RSC Adv.* **2016**, *6*, 11631–11636. [CrossRef]

51. Han, S.; Liu, K.; Hu, L.; Teng, F.; Yu, P.; Zhu, Y. Superior Adsorption and Regenerable Dye Adsorbent Based on Flower-Like Molybdenum Disulfide Nanostructure. *Sci. Rep.* **2017**, *7*, 43599. [CrossRef] [PubMed]

52. Song, H.J.; You, S.; Jia, X.H.; Yang, J. MoS$_2$ nanosheets decorated with magnetic Fe$_3$O$_4$ nanoparticles and their ultrafast adsorption for wastewater treatment. *Ceram. Int.* **2015**, *41*, 13896–13902. [CrossRef]